Green light stimulates terahertz emission from mesocrystal microspheres

X. L. Wu[1]*, S. J. Xiong[1], Z. Liu[1], J. Chen[2], J. C. Shen[1], T. H. Li[1], P. H. Wu[2] and Paul K. Chu[3]*

The discovery of efficient sources of terahertz radiation has been exploited in imaging applications[1], and developing a nanoscale terahertz source could lead to additional applications. High-frequency mechanical vibrations of charged nanostructures can lead to radiative emission, and vibrations at frequencies of hundreds of kilohertz have been observed from a ZnO nanobelt under the influence of an alternating electric field[2]. Here, we observe mechanical resonance and radiative emission at ∼0.36 THz from core–shell ZnO mesocrystal microspheres excited by a continuous green-wavelength laser. We find that ∼0.016% of the incident power is converted into terahertz radiation, which corresponds to a quantum efficiency of ∼33%, making the ZnO microspheres competitive with existing terahertz-emitting materials[1,3]. The mechanical resonance and radiation stem from the coherent photo-induced vibration of the hexagonal ZnO nanoplates that make up the microsphere shells. The ZnO microspheres are formed by means of a nonclassical, self-organized crystallization process[4–6], and represent a straightforward route to terahertz radiation at the nanoscale.

Zinc oxide (ZnO) nanostructures have a unique combination of semiconducting and piezoelectric properties[7–14]. By using the meso-crystallization pathway, core–shell ZnO mesocrystal microspheres with variable sizes that depend on synthesis time can be fabricated[6]. Figure 1a,b presents field-emission scanning electron micrographs (FE-SEM) of two typical multi-microsphere samples with microsphere diameters of 2.7 and 5.4 μm, which were fabricated with synthesis times of 3 and 10 h, respectively. The insets schematically illustrate the side- and top-view morphologies of the core and shell of a microsphere. The microsphere surface is composed of densely packed hexagonal nanoplates aligned perpendicular to the sphere and pointing to the central core (Fig. 1c). The thickness of the packed nanoplates is ∼15 nm and consistent with the coherence length D_{002} of the (002) reflection, and the ordering of the nanoplates in the shell layer increases with synthesis time. The inset in Fig. 1c depicts the FE-SEM image of a nanoplate with a hexagonal side length of ∼50 nm. The shell layer of the microsphere consists of a large number of ∼15-nm-thick flabellate nanocantilevers with lengths that depend on synthesis time. Figure 1d schematically shows a rectangular nanocantilever composed of a monolayer of hexagonal nanoplates connected to each other by poly(sodium 4-styrenesulphonate) (PSS).

Figure 2 presents the Raman vibration spectra (obtained directly on our high-resolution Raman measurement system) of five multi-microsphere samples (synthesis times: 2.5, 3, 5, 7 and 10 h) excited by the 514.5 nm line of an argon laser. The vibration signals arise from the ZnO and are not a luminescent line. In addition to the weak first-order E_{2low} mode at 2.91 THz (97 cm^{-1}) from ZnO[15], a strong vibration mode appears at 0.36 THz for all samples. The

full-width at half-maximum (FWHM) of this mode for the 10 h sample is ∼0.54 THz and increases slightly with shorter synthesis times (Fig. 2, inset).

To identify vibration coherence between the microspheres, vibration spectra were acquired from a single microsphere from each sample (representative spectra from the 10 and 3 h samples are presented in Fig. 3a,b, respectively). When compared with the spectra taken from the multi-microsphere samples, some differences are apparent. First, for the single microspheres, the peak generally shifts to a higher frequency, and the shift is larger for the microsphere produced in the shorter time. Second, for the microsphere with the longer fabrication time, the FWHM is narrower (Fig. 3a). FWHM increases as the synthesis time reduces to approach that of the 3 h multi-microsphere sample (Fig. 3b).

The origin of this terahertz vibration mode can be determined according to the microsphere structure and spectral characteristics. This vibration should be closely associated with the high-frequency vibration of the photo-induced single hexagonal ZnO nanoplate and subsequent propagation to the nanocantilevers due to elastic and electrical coupling between the nanoplates. In multi-microsphere
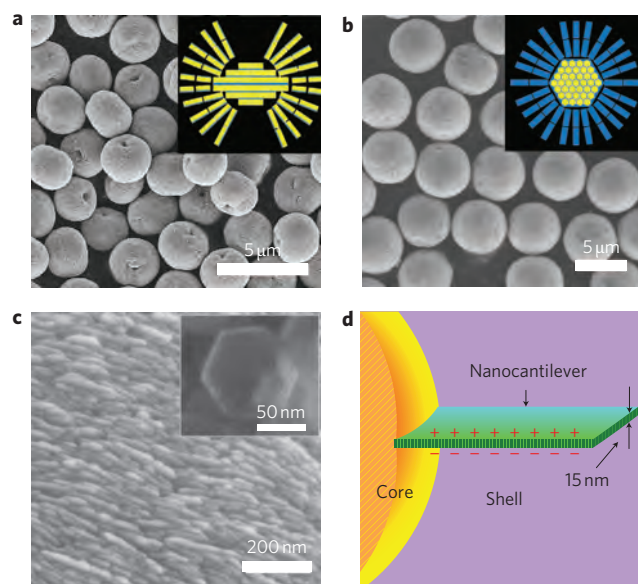

Figure 1 | FE-SEM images and schematic illustration of the ZnO mesocrystal microspheres. a,b, Microspheres fabricated with synthesis times of 3 h (**a**) and 10 h (**b**). Insets: side-view (**a**) and top-view (**b**) morphologies of the core and shell of the microsphere. **c,** High-magnification image of a microsphere surface. Inset: FE-SEM image of a hexagonal ZnO nanoplate. **d,** Schematic of a nanocantilever with thickness of 15 nm.

[1]National Laboratory of Solid State Microstructures and Department of Physics, Nanjing University, Nanjing 210093, China, [2]National Laboratory of Solid State Microstructures and Research Institute of Superconductor Electronics, Nanjing University, Nanjing 210093, China, [3]Department of Physics and Materials Science, City University of Hong Kong, Tat Chee Avenue, Kowloon, Hong Kong, China. *e-mail: hkxlwu@nju.edu.cn; paul.chu@cityu.edu.hk
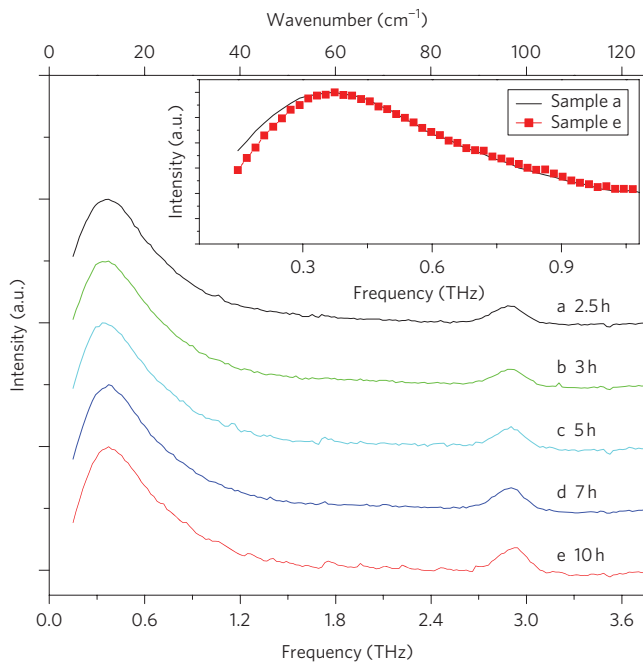
Figure 2 | Vibration spectra of the multi-microsphere samples fabricated with synthesis times of 2.5, 3, 5, 7 and 10 h. Spectra are taken from Raman scattering under excitation with the 514.5 nm line of an argon ion laser. Inset: for identification of the FWHM difference, the normalized vibration spectra of two multi-microsphere samples with synthesis times of 2.5 and 10 h are shown.
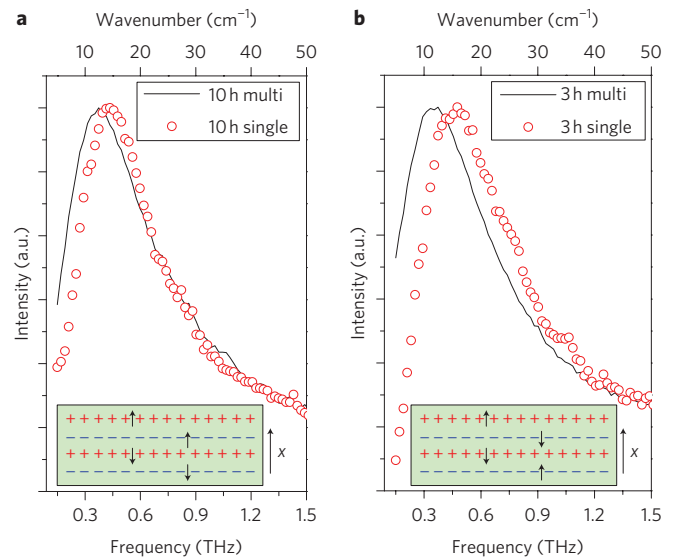

Figure 3 | Vibration spectra of single and multi-microsphere samples with different synthesis times. a,b, Data for 10 h (**a**) and 3 h (**b**) samples. Insets: stretching vibration modes in the thickness direction of a nanoplate with frequencies ν_1 (**a**) and ν_2 (**b**). Black arrows show the vibration directions in different layers and $+/-$ signs indicate charges in the Zn and O layers.

systems, as a result of contacts between the microspheres, vibrations excited locally by the laser can propagate to the whole system. This results in the disappearance of the size effect and the emergence of a single frequency feature that is independent of the size of a single microsphere. This is the reason why all the modes in spectra a–e of Fig. 2 have almost the same frequency, despite the fact that the microsphere sizes are different. Because contacts between the microspheres are not complete, different nanocantilever lengths can still affect vibration frequency slightly. For microspheres produced in shorter times, the arrangement of nanocantilevers in the shell layer is less ordered, so the FWHM is slightly larger (Fig. 2, inset).

In a single microsphere, one end of the nanocantilever is free and the other end is in contact with the core. Propagation of vibration within the sphere is therefore limited, and frequency is affected by size. This frequency will be larger when the nanocantilever is shorter, as illustrated in Fig. 3a,b, which shows that the dimensions of the microsphere in the 3 h sample are smaller than those of the 10 h sample. In addition, because the nanocantilever arrangement in the 10 h microsphere has better ordering than the 3 h microsphere, the FWHM is narrower. Similarly, ordering of the nanocantilever arrangement in the 10 h sample is better in a single microsphere than in multi-microspheres, and so the FWHM is narrower in the single microsphere (Fig. 3a). For the 3 h microspheres, the nanocantilever arrangement in a single microsphere has large disorder, so the FWHM is the same as that of the multi-microspheres.

The basic structure of the system is a nanoplate. If one considers the stretching vibrations in the thickness or x-direction (Fig. 3, inset) and two free surfaces at $x = 0$ and $x = h$ (where h is the thickness), we obtain from the dynamical equation the eigenfrequencies $\nu_n = n\alpha/2h$ (where $n = 1, 2, \ldots$) and corresponding vibration functions $\varphi_n(x) = A_n \cos(\pi nx/h)$, where $\alpha = \sqrt{(E_0/\rho)}$, E_0 is Young's modulus, ρ is density, and A_n is amplitude. Mode ν_1 (shown in the inset of Fig. 3a) is infrared active, but Raman inactive. The lowest Raman active mode is ν_2 (Fig. 3b, inset). For ZnO,

$\rho = 5.6$ g cm^{-3}, $E_0 = 140$ GPa (ref. 16), and the thickness of the nanoplates is 15 nm, giving $\nu_2 \approx 0.33$ THz, which is independent of the shape and area of the nanoplates and consistent with the frequency of 0.36 THz observed for the multi-microsphere system.

Many nanoplates are assembled to form a nanocantilever and many nanocantilevers are in turn attached to the centre of the sphere. This leads to coherent vibrations of the ν_2 modes. If the nanoplates are arranged as a square lattice in the nanocantilevers and we only consider nearest-neighbour coupling, the frequencies of the collective vibration modes can be calculated as $\nu(k_1, k_2) \approx \sqrt{[\nu_2^2 + \eta^2(2 - \cos k_1 - \cos k_2)]}$, where η describes the average coupling strength depending on binders between the nanoplates, and k_1 and k_2 are wave vectors in two directions. The modes with the smallest k_1 and k_2 (the longest wavelengths) are mostly Raman active. However, the smallest wave vectors are limited by the sphere size and their values can be estimated as $k_{1,2} \approx 2\pi/l_{1,2}$, where $l_{1,2}$ is the number of nanoplates included in the corresponding directions. Based on the structures shown in Fig. 1, we have $l_1 = l_2 \approx 20$ and $l_1 = l_2 \approx 26$ for the 3 and 10 h samples, and can then obtain the frequencies $\nu = 0.41$ THz and 0.46 THz, respectively, if the coupling strength is $\eta = 1$ THz.

For the multiple microspheres, the spheres are in contact with one another, forming a larger structure. This removes the limitation for the smallest wave vectors, so that $k_{1,2} \to 0$ and $\nu \to \nu_2$, independent of the size of the microspheres. This effect is observed from our experiments (Fig. 2); details regarding theoretical calculations are described in the Supplementary Information.

To determine the suitability of the ZnO microsphere as a practical terahertz source, we measure the terahertz radiation of the typical 10 h microsphere sample. Figure 4a presents a schematic of the experimental setup. The terahertz radiation power W_{out} exhibits a good linear dependence on input laser power W_{in} (Fig. 5a) without any indication of saturation in the investigated range. The output terahertz power can even reach 6.8 μW if the output power is not saturated, as demonstrated in our Raman measurements. This implies that the terahertz radiation power can be tuned easily over a wide range by changing the input power. Figure 5b shows the dependence of the output power on the detection distance d under an excitation power of 36 mW. The output power decreases
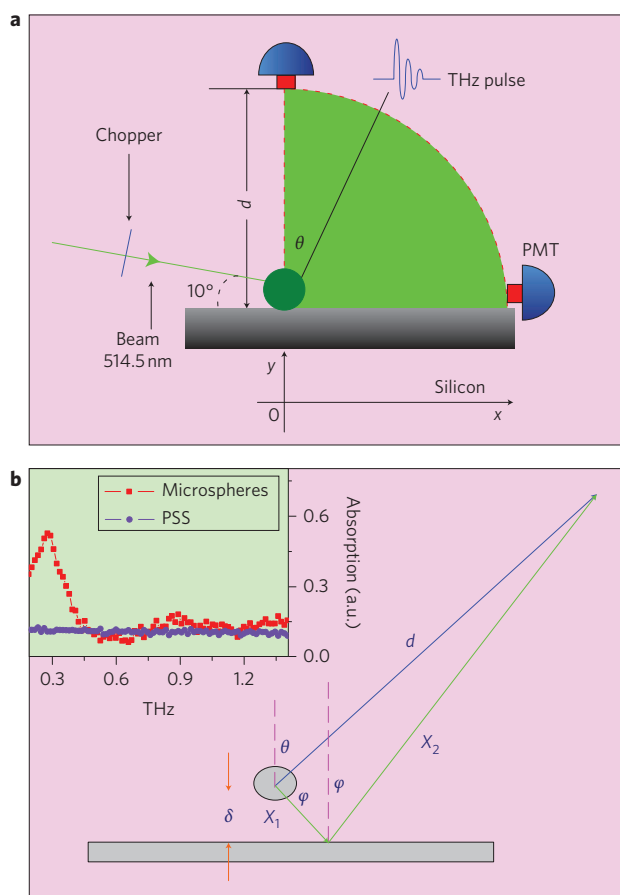
Figure 4 | Experimental setup and terahertz absorption spectra.
a, Experimental setup for measuring terahertz radiation. PMT, terahertz detector, with a collection area of $\pi \times 5^2$ mm^2. **b**, Schematic of two-path interference from a point source to a detector. Inset: terahertz absorption spectra obtained from the 10 h multi-microsphere sample and the organic additives, PSS, respectively. An infrared active mode from the microsphere sample is observed at 0.288 THz.

36 mW. The oscillation in the curve reflects some effects of interference, which will be analysed in the following. A detailed method for the calculation of total light radiation power has been given previously[17,18]. Because of reflection at the silicon surface, the total terahertz power W_{out} can simply be obtained by integrating the hemisphere above the substrate, $W_{out} = 2\pi d^2 \int_0^{\pi/2} w_{out}(\theta) \sin\theta \, d\theta$, where $w_{out}(\theta)$ is the power density per unit area at the measurement point. By dividing W_{out} by the total input laser power on the spot, the efficiency of the terahertz generation is calculated to be 0.016%. In other words, the quantum efficiency in converting a green photon into a 0.36 THz photon is ~33%, which is greater than that observed from traditional semiconducting nanostructures such as Si (5%)[19], 3C–SiC (17%)[20], or II–VI group quantum dots (21%)[21], thereby demonstrating the practicality of using ZnO microspheres as a terahertz source.

Furthermore, ZnO microspheres can be used as an ideal terahertz point source, as the effective size can be reduced to that of a single microsphere. The oscillation in Fig. 5c is a result of interference between two paths from a single point source. As illustrated in Fig. 4b, there are two paths from the point source to the detector: a direct path d and another path via reflection at the silicon substrate surface $x_1 + x_2$. From the interposition of these two components[17,18], the interference leads to the θ-dependent power density $w_{out}(\theta) \propto \cos^2[\pi(x_1 + x_2 - d)/\eta_0]$, where η_0 is the wavelength, $x_1 = \delta/\cos\varphi$ and $x_2 = (d\cos\theta + \delta)/\cos\varphi$, where δ is the height of the point source above the substrate and angle φ is determined by $\cos 2\varphi = (4\delta^2 + 4\delta d\cos\theta + d^2\cos 2\theta)/(d^2 + 4\delta d\cos\theta + 4\delta^2)$. From this formula, the oscillation in Fig. 5c can be fitted by setting $d = 1.8$ cm, $\delta = 0.126$ cm and $\eta_0 = 0.09$ cm. These parameters reflect the realistic situation in the experiments.

Mesocrystal core–shell microspheres represent an experimentally simple and efficient vehicle for generating terahertz radiation. It may be possible to increase their efficiency by adopting effective mirror reflection or designing hierarchical nanostructures, and their integration into nanoscale devices may allow novel applications like microscale medical imaging and micro-displacement driving.

Methods

Synthesis. Core–shell structured ZnO mesocrystal microspheres were synthesized using a facile one-pot hydrothermal method in the presence of the water-soluble polymer PSS[6]. Microsphere dimensions and nanocantilever lengths were controlled by selecting different durations of synthesis time. Multiple microsphere samples for Raman measurements were prepared by putting a trace of microsphere powder on a single-crystal silicon wafer with a thickness of 1.0 mm. SEM observations indicate that powder thickness was in the range of 5–30 μm (ref. 6). To obtain a single microsphere sample we placed a small amount of ZnO microsphere powder into an aqueous solution, then applied ultrasonic vibration for 10 min. A drop of the

with d as the terahertz radiation comes out from a 'point' source corresponding to the radiating spot of the sample. Figure 5c exhibits the dependence of the output power density per unit area at $d = 1.8$ cm on deviating angle θ under an excitation power of
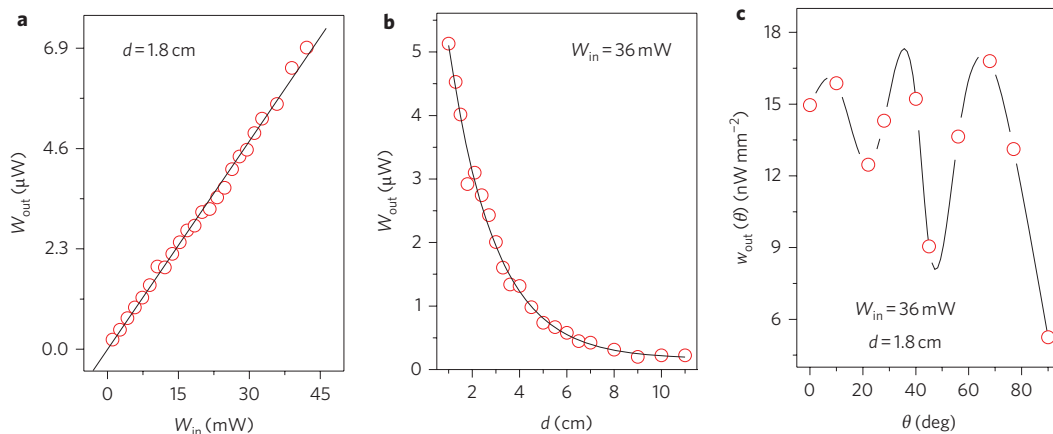

Figure 5 | Dependence on different parameters of terahertz radiation power for the 10 h microsphere sample. a,b, Dependence of W_{out} on incident laser power W_{in} (**a**) and detection distance d (**b**). **c**, Dependence of terahertz radiation power density $w_{out}(\theta)$ on deviating angle θ. Average uncertainty in terahertz radiation power is ~10%.

suspension was put on the silicon substrate and we searched for a microsphere on which to carry out measurements. To measure terahertz radiation, multiple microspheres were attached to the silicon wafer with a twin adhesive polymer with a thickness of ~1 mm. Note that our Raman measurements did not reveal a similar low-frequency Raman peak from the adhesive.

Analysis. Raman vibration spectra were obtained on a T64000 triple Raman system with a micro-Raman backscattering geometry using the 514.5 nm line of an argon ion laser as the excitation source. The diameter of the beam spot was 5 µm, and the power illuminating the sample could be adjusted from 0 to 20 mW. The measurement was conducted at room temperature without the polarization configuration, and the resolution of the spectrometer was 0.1 cm^{-1}. The acquired spectra were the same as those taken under excitation by the 488 nm line. The high resolution and rejection rate of this measurement system allowed observation of the vibration signals close to the Rayleigh line to less than 0.15 THz (5 cm^{-1})[22,23]. We also acquired the terahertz absorption spectra of the microspheres on a traditional transmitted terahertz time-domain spectroscopy system (Ekspla)[24], and an infrared active mode at a lower frequency of ~0.288 THz was obtained (Fig. 4b, inset)[25]. No corresponding terahertz vibration signals occurred for the organic additives, polymer PSS.

We used the 514.5 nm line of an argon ion laser as the excitation source to acquire the terahertz radiation (Fig. 4a). The illumination power was adjusted from 0 to 50 mW. The incident beam, expanded to an area of $\pi \times (5/2)^2$ mm^2, illuminated the microsphere sample with an angle of 10° to the silicon substrate plane. To obtain pulsed terahertz radiation, we used a chopper (SR540, Stanford Research Systems) with a rotating frequency of 10 revolutions per second to convert the continuous visible light into a pulsed wave. A Golay Cell terahertz detector (Microtech Instruments) with a spectral range of 0.02–20 THz, connected to an NF 5600A single phase lock-in amplifier (NF Electronic Instruments), was used in the terahertz radiation measurement. The terahertz detector was calibrated using the 'hot–cold load' method[26]. During detection of the terahertz radiation, a Yoshinaga low-pass filter (<1.5 THz) was used to suppress the green pump light and thermal radiative power by more than 90% (ref. 27), also suppressing more than 90% of the terahertz radiation signal higher than 1.5 THz. As the emission intensity at 2.9 THz is far lower than that at 0.36 THz (Fig. 2), the influence of the 2.9 THz radiation is negligible. To further suppress the green light, we added four layers of black polyethylene film on the entrance of the detector, such that the green pump signal became almost undetectable. Finally, to ensure that we could accurately measure the radiation from the samples without thermal background radiation and residual green pump signal, we conducted the same measurement on a commercial ZnO powder sample with particle sizes of 1–5 µm and attached on the same silicon wafer to obtain a reference radiation signal. This reference signal was subtracted from the final results for the microsphere samples. By changing the incident laser power W_{in}, detection distance d and deviating angle θ, we obtained the dependence of the pulsed output terahertz power W_{out} on these parameters. Note that the use of the four polyethylene films also reduced the obtained terahertz power reading due to Fresnel reflection losses (increasing with incident angle). This caused the practical terahertz output power to increase by ~10% and the quantum efficiency to reach ~37%.

References

1. Chan, W. L., Deibel, J. & Mittleman, D. M. Imaging with terahertz radiation. *Rep. Prog. Phys.* **70,** 1325–1379 (2007).
2. Bai, X. D., Gao, P. X., Wang, Z. L. & Wang, E. G. Dual-mode mechanical resonance of individual ZnO nanobelts. *Appl. Phys. Lett.* **82,** 4806–4808 (2003).
3. Siegel, P. Terahertz technology. *IEEE Trans. Microw. Theory Tech.* **50,** 910–928 (2002).
4. Cölfen, H. & Antonietti, M. Mesocrystals: inorganic superstructures made by highly parallel crystallization and controlled alignment. *Angew. Chem. Int. Ed.* **44,** 5576–5591 (2005).
5. Cölfen, H. & Antonietti, M. *Mesocrystals and Nonclassical Crystallization* (Wiley, 2008).
6. Liu, Z. *et al.* Intrinsic dipole-field-driven mesoscale crystallization of core–shell ZnO mesocrystal microspheres. *J. Am. Chem. Soc.* **131,** 9405–9412 (2009).
7. Wang, Z. L. & Song, J. Piezoelectric nanogenerators based on zinc oxide nanowire arrays. *Science* **312,** 242–246 (2006).
8. Wang, Z. L. *et al.* Semiconducting and piezoelectric oxide nanostructures induced by polar surfaces. *Adv. Funct. Mater.* **14,** 943–956 (2004).
9. Özgür, Ü. *et al.* A comprehensive review of ZnO materials and devices. *J. Appl. Phys.* **98,** 041301 (2005).
10. Kulkarni, A. J., Zhou, M. & Ke, F. J. Orientation and size dependence of the elastic properties of zinc oxide nanobelts. *Nanotechnology* **16,** 2749–2756 (2005).
11. Song, J. H., Wang, X. D., Riedo, E. & Wang, Z. L. Elastic property of vertically aligned nanowires. *Nano Lett.* **5,** 1954–1958 (2005).
12. Cao, G. X. & Chen, X. Energy analysis of size-dependent elastic properties of ZnO nanofilms using atomistic simulations. *Phys. Rev. B* **76,** 165407 (2007).
13. Zhao, M. H., Ye, Z. Z. & Mao, S. X. Photoinduced stiffening in ZnO nanobelts. *Phys. Rev. Lett.* **102,** 045502 (2009).
14. Zhang, L. X. & Huang, H. C. Young's moduli of ZnO nanoplates: *ab initio* determinations. *Appl. Phys. Lett.* **89,** 183111 (2006).
15. Yang, L. W., Wu, X. L., Huang, G. S., Qiu, T. & Yang, Y. M. *In situ* synthesis of Mn-doped ZnO multileg nanostructures and Mn-related Raman vibration. *J. Appl. Phys.* **97,** 014308 (2005).
16. Kobiakov, I. B. Elastic, piezoelectric and dielectric properties of ZnO and CdS single crystals in a wide range of temperatures. *Solid State Commun.* **35,** 305–310 (1980).
17. Lukosz, W. & Kunz, R. E. Light emission by magnetic and electric dipoles close to a plane interface. I. Total radiated power. *J. Opt. Soc. Am.* **67,** 1607–1615 (1977).
18. Lukosz, W. & Kunz, R. E. Light emission by magnetic and electric dipoles close to a plane interface. II. Total radiated power. *J. Opt. Soc. Am.* **67,** 1615–1619 (1977).
19. Fauchet, P. M. *et al.* Light-emitting porous silicon: materials science, properties, and device applications. *IEEE J. Sel. Top. Quantum Electron.* **1,** 1126–1139 (1995).
20. Fan, J. Y. *et al.* 3C–SiC nanocrystals as fluorescent biological labels. *Small* **4,** 1058–1062 (2008).
21. Bruchez, M. Jr, Moronne, M., Gin, P., Weiss, S. & Alivisatos, A. P. Semiconductor nanocrystals as fluorescent biological labels. *Science* **281,** 2013–2016 (1998).
22. Wu, X. L., Xiong, S. J., Sun, L. T., Shen, J. C. & Chu, P. K. Low-frequency Raman scattering from nanocrystals caused by coherent excitation of phonons. *Small* **5,** 2823–2826 (2009).
23. Courty, A., Mermet, A., Albouy, P. A., Duval, E. & Pileni, M. P. Vibration coherence of self-organized silver nanocrystals in f.c.c. supra-crystals. *Nature Mater.* **4,** 395–398 (2005).
24. Zhang, C. H., Jin, B. B., Chen, J., Wu, P. H. & Tonouchi, M. Noncontact evaluation of nondoped InP wafers by terahertz time-domain spectroscopy. *J. Opt. Soc. Am. B* **26,** A1–A5 (2009).
25. Ristić, M., Ivanda, M., Popović, S. & Musić, S. Dependence of nanocrystalline SnO$_2$ particle size on synthesis route. *J. Non-Cryst. Solids* **303,** 270–280 (2002).
26. Tiuri, M. E. Radio astronomy receivers. *IEEE Trans. Military Electron.* **8,** 264–272 (1964).
27. Yamada, Y., Mitsuishi, A. & Yoshinaga, H. Transmission filters in the far-infrared region. *J. Opt. Soc. Am.* **52,** 17–19 (1962).

Author contributions

X.L.W. designed the experimental setup, performed the experiments, analysed the data, and co-wrote the manuscript. S.J.X. analysed the data and co-wrote the manuscript. Z.L. and J.C.S. performed the experiments. J.C. and P.H.W. designed the experimental setup and analysed the data. T.H.L. plotted all the figures. P.K.C. analysed the data and co-wrote the manuscript.

Additional information

The authors declare no competing financial interests. Supplementary information accompanies this paper at www.nature.com/naturenanotechnology. Reprints and permission information is available online at http://npg.nature.com/reprintsandpermissions/. Correspondence and requests for materials should be addressed to X.L.W. and P.K.C.

Green light stimulates terahertz emission from mesocrystal

microspheres

X. L. Wu, S. J. Xiong, Z. Liu, J. Chen, J. C. Shen, T. H. Li, P. H. Wu, and Paul K. Chu

Considering the stretching vibrations in the thickness (x) direction of a nanoplate (insets, Fig. 3), the displacement $u(x,t)$ satisfies equation

$$\frac{\partial^2 u(x,t)}{\partial t^2} - \alpha^2 \frac{\partial^2 u(x,t)}{\partial x^2} = 0, \tag{1}$$

where $\alpha = \sqrt{\dfrac{E_0}{\rho}}$ and E_0 and ρ are the Young's modulus and density, respectively.

Separating the variables in $u(x,t)$ with $u(x,t) = \phi(x)q(t)$, we have

$$\frac{d^2\phi(x)}{dx^2} + \frac{(2\pi\nu)^2}{\alpha^2}\phi(x) = 0,$$

and

$$\frac{d^2 q(t)}{dt^2} + (2\pi\nu)^2 q(t) = 0,$$

where ν is the frequency. The general solution can be written as

$$\phi(x)q(t) = e^{2\pi i \nu t}\left(C_1 \sin\frac{2\pi\nu x}{\alpha} + C_2 \cos\frac{2\pi\nu x}{\alpha} \right),$$

where C_1 and C_2 are integration constants. Since two surfaces at $x = 0$ and $x = h$ (h being the thickness) of the nanoplate are free, we have the boundary conditions for $\phi(x)$:

$$\left.\frac{d\phi(x)}{dx}\right|_{x=0} = \left.\frac{d\phi(x)}{dx}\right|_{x=h} = 0.$$

By substituting the general solution into the boundary conditions and according to the existence of nonzero solutions, we obtain the eigenfrequencies

$$\nu_n = \frac{n\alpha}{2h}, \qquad n = 1, 2, ... \tag{2}$$

and corresponding vibration functions

$$\phi_n(x) = A_n \cos\left(\frac{\pi n x}{h}\right). \tag{3}$$

In a microsphere, many nanoplates are assembled to form a nanocantilever and then many nanocantilevers are attached to the center of the sphere.   We can adopt the ν_2 modes of the nanoplates as the basic ones to analyze the coherent vibrations in the microsphere.   Hence, the amplitude in Eq. (3) denoted as A_{2i} for the ith nanoplate can be viewed as the generalized coordinate.   The kinetic energy of the system is

$$K = 2\pi^2 \nu^2 \sum_i m_i A_{2i}^2,$$

where $m_i = \frac{\rho h S_i}{2}$ and S_i being the area of the nanoplate is the equivalent mass of the mode.   The elastic energy includes those of the individual nanoplates and the coupling terms

$$V = 2\pi^2 \nu_2^2 \sum_i m_i A_{2i}^2 + \frac{1}{2} \sum_{i \neq j} \lambda_{ij} (A_{2i} - A_{2j}),$$

where λ_{ij} is the coupling strength between plates i and j.   If the nanoplates are arranged as a square lattice in the nanocantilevers and we only consider the nearest neighbor coupling, the frequencies of the collective vibration modes can be written as

$$\nu(k_1, k_2) \approx \sqrt{\nu_2^2 + \eta^2(2 - \cos k_1 - \cos k_2)},$$

where $\eta = \left\langle \sqrt{\frac{\lambda_{ij}}{2\pi^2 m_i}} \right\rangle$ describes the average coupling strength depending on the organic binders between nanoplates, k_1 and k_2 are wave vectors of the collective modes in the two directions.